ISSN: 2688-8645

Nonlinear Vibration Analysis of Bearing-Rotor Systems with Ball Defects Considering Time-Varying Displacement Excitation

Hui Wang [1], Zhenning Su [1], Chang Liu [1], Fancheng Meng [1], Bo Song [1,*] and Shiying Zhang [2]

[1] Ccteg Shenyang Engineering Company, Shenyang, Liaoning, China

[2] Shenyang Jianzhu University, Shenyang, Liaoning, China

* Corresponding author: Bo Song

Abstract

Bearing-rotor systems are of critical significance to advanced rotating equipment. However, under high-speed operating conditions, defects may occur on the ball surfaces due to increased contact stresses. To understand the influence of ball surface defect on the bearing-rotor systems, the time-varying displacement excitation is proposed. Defect size changes contact deformation in the bearing. The contact force is changed as a result. These factors are incorporated into the dynamic model. The model describes a bearing-rotor system with a defect-ball bearing. Bifurcation diagrams is employed, the influence of speed and defect dimensions on the system's nonlinear vibration is examined. Experimental validation is conducted through vibration testing. The results show that the occurrence of ball defects has a notable effect on the system's motion behavior. With the increase in the size of ball defects, the amplitudes of the relevant frequencies f_b, f_c and their combined frequencies in the spectrum increase. Strong alignment is seen between experimental and simulated outcomes, and the amplitude error of the ball impact frequency is 4.9%. This study provides a framework for analyzing the dynamics of bearing-rotor systems.

Keywords

Bearing-rotor Systems; Defect-ball; Dynamic Model; Time-varying Displacement.

1. Introduction

The bearing rotor system (BRS) is an important component of rotating machinery. They are widely used in aerospace, CNC machine tools and other high-end manufacturing fields [1]. However, due to manufacturing defects and high-intensity operation, local defect such as pits, spalling and scratches may occur on the raceway or ball surface. These defects significantly reduce the running accuracy of the bearing. This affects the contact characteristics of bearing components, aggravating nonlinear vibration and reducing BRS stability [2]. Therefore, it is crucial to investigate the dynamic behaviors and nonlinear vibration mechanisms of bearing with the combined effects of local defect.

When a local defect on a bearing component interacts with its mating component, a sudden change occurs in the interface clearance. This clearance nonlinearity introduces complex nonlinear responses to the system. In recent years, to investigate the fault mechanism of bearings with local defects, numerous scholars have developed dynamic models for BRS featuring defects at different locations. Liu et al. [3] proposed two excitation functions. One was a time-varying displacement (TVD) accounting for defect edge expansion. The other was a time-varying stiffness describing defect morphology. They discovered that the length of defects has a notable impact on acceleration peaks. Cao et al. [4] considered the additional deflection

ISSN: 2688-8645

caused by defects and the change in contact force direction. They presented modeling approaches for single defects, multiple defects and composite faults. These methods demonstrate high accuracy. Patel et al. [5] developed a new bearings dynamic model. This model integrated roller tilt deformation and the coupling effects of multiple types of defects. Through this model, they revealed the evolutionary law of periodic-chaotic dynamic characteristics. Li et al. [6] constructed a five-degree-of-freedom bearings dynamic model. This model incorporated clearance fits, defect evolution and time-varying characteristics of contact forces. They verified that the attenuation effect of clearance on contact forces is far less pronounced than that exerted by defects. Sameera et al. [7] developed a bearing dynamic model with outer ring extended defects. This model integrates time-varying stiffness and impact force excitation mechanisms. It enabled high-precision diagnosis of five defect sizes.

In high-speed operation of bearings, local defects tend to form on ball surfaces. These defects may result from manufacturing flaws or contact fatigue. Such defects cause abnormal concentration of Hertzian contact stress. This leads to periodic impact vibrations. Ultimately, it accelerates the deterioration of bearing precision and may even trigger system failure. To address this issue, a TVD model for ball defect generation were established. These were incorporated into the bearing-rotor dynamic model. The effects of the size of bearing defects and speed on the vibration characteristics of the (BRS) were systematically analyzed. Experimental validation confirmed that the model exhibits high accuracy. The proposed model supplies theoretical support for bearing health monitoring and the evaluation of dynamic characteristics.

2. Dynamic Model of BRS with A Ball Defect

During the bearing's actual operation, the relative positional relationships among the cage, balls, inner raceway and outer raceway within the bearing will undergo dynamic changes due to the interactions among them. Figure 1 depicts the interactive configuration of the internal components within the bearing. The coordinate system (O-xyz), established at the bearing center, serves to quantify the displacement of the bearing inner race along the x, y and z axes. Correspondingly, the ball's displacement along the x_b, y_b and z_b directions is described by the coordinate system at the ball's center (O_b-$x_by_bz_b$). Additionally, ω_x, ω_y and ω_z stand for the ball's respective angular velocities around the x_b, y_b and z_b axes. While the inner ring spins at an angular speed of ω, the outer ring remains motionless.

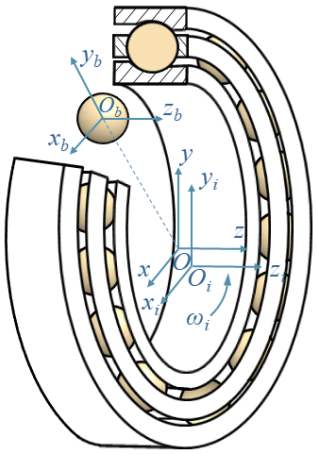

Fig 1. Coordinate system diagram of the bearing

During the operation of the bearing, the TVD is given by

ISSN: 2688-8645

$$u_f = \begin{cases} H = \begin{cases} \frac{D_w}{2}(1-\cos\theta_b), 0 \le \theta_b \le \frac{\theta_R}{2} \\ \frac{D_w}{2}(1-\cos(\theta_R-\theta_b)), \frac{\theta_R}{2} < \theta_b \le \theta_R \end{cases} \\ 0, others \end{cases} \tag{1}$$

where θ_b is the ball defect area rotational angle on the raceway.

In accordance with Hertz contact theory and incorporating damping effects, the bearing total contact force is given by

$$\begin{cases} f_x = c_n \dot{x} + \sum_{j=1}^{N_b} k_n \left(x\cos\theta_j + y\sin\theta_j - u - u_f \right)^{1.5} \cos\theta_j \\ f_y = c_n \dot{y} + \sum_{j=1}^{N_b} k_n \left(x\cos\theta_j + y\sin\theta_j - u - u_f \right)^{1.5} \sin\theta_j \end{cases} \tag{2}$$

where u is the radial internal clearance, θ_j denotes the angular position of the j-th ball, and the TVD of the non-defective ball is 0, c_n stands for proportional damping, k_n is the bearing contact stiffness coefficient, which can be expressed as

$$k_n = \frac{1}{\left(k_i^{-3/2} + k_o^{-3/2} \right)^{2/3}} \tag{3}$$

where k_i is the contact stiffness coefficients of the inner ring, k_o denote the contact stiffness coefficients of outer ring, which can be given by

$$\begin{cases} k_i = \frac{2^{2.5}\left(\Sigma\rho_i\right)^{-0.5}}{3\Gamma_i^{1.5}} \left(\frac{1-v_b^2}{E_b} + \frac{1-v_i^2}{E_i} \right)^{-1} \\ k_o = \frac{2^{2.5}\left(\Sigma\rho_o\right)^{-0.5}}{3\Gamma_o^{1.5}} \left(\frac{1-v_b^2}{E_b} + \frac{1-v_o^2}{E_o} \right)^{-1} \end{cases} \tag{4}$$

where v_o is the Poisson's ratios of the outer ring materials, v_i is the Poisson's ratios of the inner ring materials, and E_o is the elastic moduli of the outer ring materials, E_i is the elastic moduli of the inner ring materials.

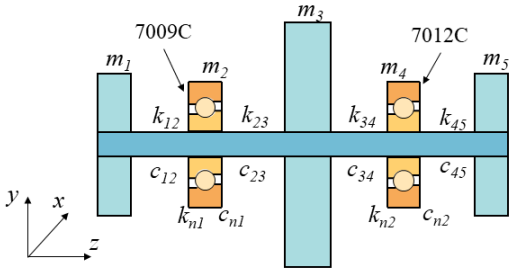

Fig 2. Simplified diagram of the BRS

To establish a strong coupling between the bearing and the rotor system and to facilitate a more intuitive understanding of bearing defect, the contact force model of the bearing can be incorporated into the rotor system. Consequently, the vibration signals associated with bearing defect are embedded within the BRSs. This integration enables direct simulation of various bearing operating conditions. However, in practice, it is difficult to model the dynamics of the ball due to its unpredictable rotation path. The model is simplified by making the following assumptions:

ISSN: 2688-8645

1. The bearing outer ring does not rotate.
2. The center of mass of each component aligns with its geometric center.
3. The system operates steadily.
4. It is assumed that the ball damage mode presents a regular plane linked to the defect width.

The BRS is supported by angular contact ball bearings at both ends. To simplify the research work, the lumped mass method is employed to simplify the system into five lumped mass elements and four elastic shaft segments. Fig. 2 depicts the simplified structure of the BRS. For the simplified BRS, its dynamic differential equations may be given by

$$\begin{cases} m_1\ddot{x}_1 + c_{12}\left(\dot{x}_1 - \dot{x}_2\right) + k_{12}\left(x_1 - x_2\right) = m_1 e\omega^2 \cos\omega t \\ m_1\ddot{y}_1 + c_{12}\left(\dot{y}_1 - \dot{y}_2\right) + k_{12}\left(y_1 - y_2\right) = -m_1 g + m_1 e\omega^2 \sin\omega t \\ m_2\ddot{x}_2 + \left(c_{12} + c_{23}\right)\dot{x}_2 - c_{12}\dot{x}_1 - c_{23}\dot{x}_3 + \left(k_{12} + k_{23}\right)x_2 - k_{12}x_1 - k_{23}x_3 = -f_{x2} \\ m_2\ddot{y}_2 + \left(c_{12} + c_{23}\right)\dot{y}_2 - c_{12}\dot{y}_1 - c_{23}\dot{y}_3 + \left(k_{12} + k_{23}\right)y_2 - k_{12}y_1 - k_{23}y_3 = -m_2 g - f_{y2} \\ m_3\ddot{x}_3 + \left(c_{23} + c_{34}\right)\dot{x}_3 - c_{23}\dot{x}_2 - c_{34}\dot{x}_4 + \left(k_{23} + k_{34}\right)x_3 - k_{23}x_2 - k_{34}x_4 = m_3 e\omega^2 \cos\omega t \\ m_3\ddot{y}_3 + \left(c_{23} + c_{34}\right)\dot{y}_3 - c_{23}\dot{y}_2 - c_{34}\dot{y}_4 + \left(k_{23} + k_{34}\right)y_3 - k_{23}y_2 - k_{34}y_4 = -m_3 g + m_3 e\omega^2 \sin\omega t \\ m_4\ddot{x}_4 + \left(c_{34} + c_{45}\right)\dot{x}_4 - c_{34}\dot{x}_3 - c_{45}\dot{x}_5 + \left(k_{34} + k_{45}\right)x_4 - k_{34}x_3 - k_{45}x_5 = -f_{x4} \\ m_4\ddot{y}_4 + \left(c_{34} + c_{45}\right)\dot{y}_4 - c_{34}\dot{y}_3 - c_{45}\dot{y}_5 + \left(k_{34} + k_{45}\right)y_4 - k_{34}y_3 - k_{45}y_5 = -m_4 g - f_{y4} \\ m_5\ddot{x}_5 + c_{45}\left(\dot{x}_5 - \dot{x}_4\right) + k_{45}\left(x_5 - x_4\right) = m_5 e\omega^2 \cos\omega t \\ m_5\ddot{y}_5 + c_{45}\left(\dot{y}_5 - \dot{y}_4\right) + k_{45}\left(y_5 - y_4\right) = -m_5 g + m_5 e\omega^2 \sin\omega t \end{cases} \tag{5}$$

where m_i represent the centralized mass, c_{ij} is the damping coefficients between each of the centralized masses, k_{ij} is the stiffness coefficients between each of the centralized masses, e is the unbalanced eccentricity. To establish a coupling relationship between deformation and stiffness, the effects of the TVD and radial displacement are incorporated into the bearing contact force model, eliminating the limitation that supporting force depends solely on inner race deformation. The BRS is fitted with angular contact bearings at its front and rear ends, specifically of the 7009C and 7012C, with their detailed structural dimensions presented in table 1. Solving the dynamic equations proves challenging when parameters are calculated in international units, owing to significant discrepancies in their orders of magnitude. To determine suitable error control values and step sizes, all parameters are nondimensionalized and standardized to a unit of 1.

Table 1. Bearing parameters

Bearing type	7009C	7012C
inner diameter (mm)	45	60
inner raceway diameter (mm)	51.3	65.2
ball diameter (mm)	8.7	9.6
outer diameter (mm)	75	95
outer raceway diameter (mm)	68.8	85.7
initial contact angle (°)	15	15

3. Simulation Analysis

During the BRS's operation, the impact of TVD excitation generated by local bearing faults on the entire system's nonlinear vibration should not be neglected. Taking a rotor system with a 7009C bearing with ball defects at one end and a healthy 7012C bearing at the other end as an example.

ISSN: 2688-8645

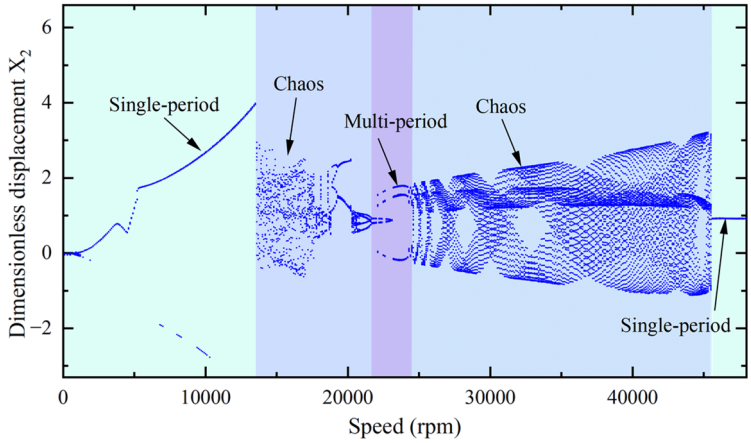

Fig 3. The BRS bifurcation diagram

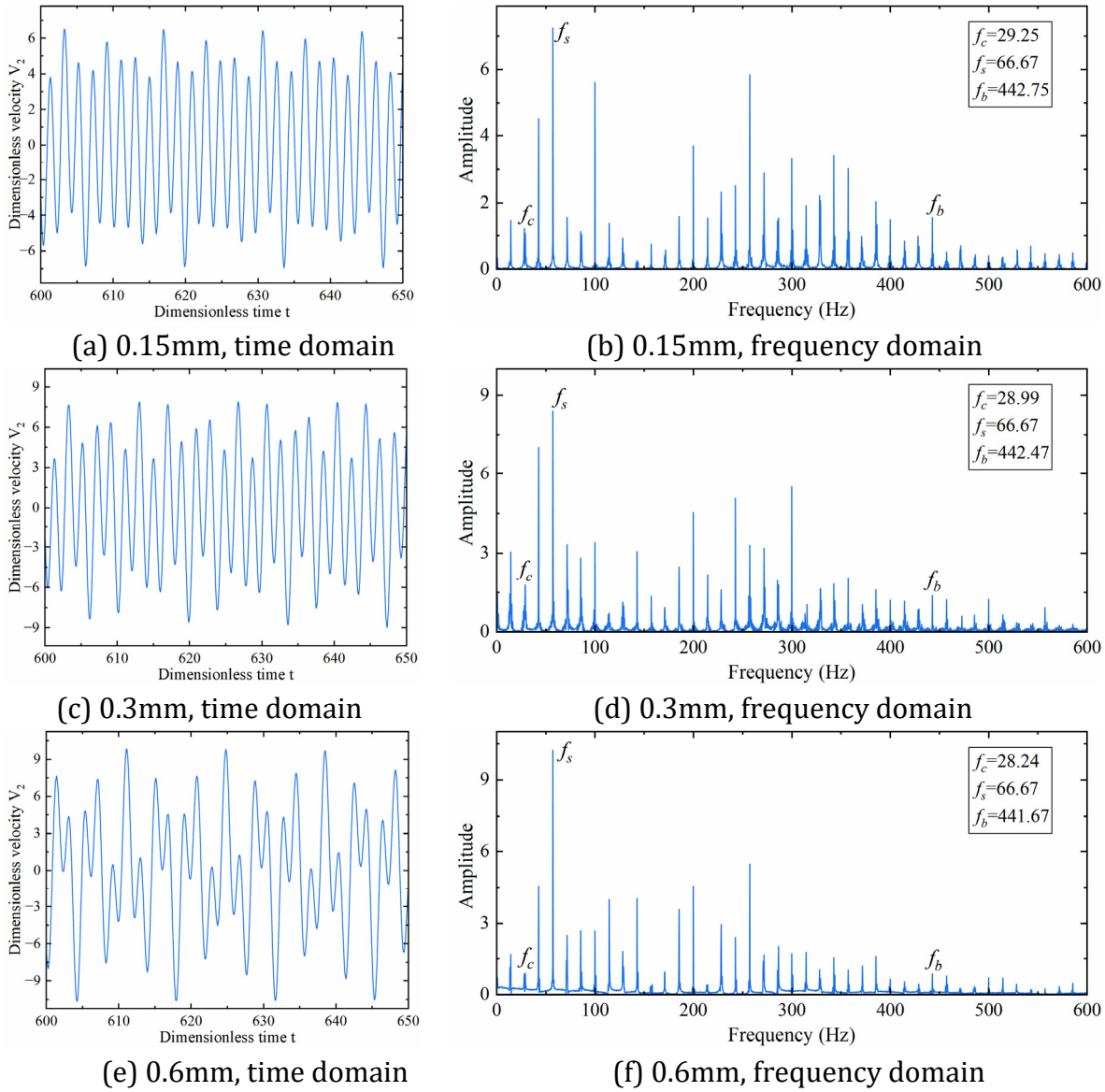

(a) 0.15mm, time domain (b) 0.15mm, frequency domain

(c) 0.3mm, time domain (d) 0.3mm, frequency domain

(e) 0.6mm, time domain (f) 0.6mm, frequency domain

Fig 4. Vibration response of different defect sizes

The Fig. 3 depicts the BRS bifurcation diagram with a ball defect size of 0.15 mm. When the speed is below 13500 rpm, the BRS mainly exhibits single-period motion, and additionally, a quasi-periodic state emerges. In the range of 13500–21600 rpm, the BRS motion is relatively

ISSN: 2688-8645

complex, manifesting as chaotic motion. In the range of 21600–24300 rpm, the system exhibits the phenomenon of inverse bifurcation within this interval, showing motion characteristics with multiple periods. When the speed exceeds 24300 rpm, chaotic motion reappears in the system. Only when the speed reaches 45600 rpm does the system return to single-period motion. The reason for such alternating motion patterns lies in the contact force nonlinear characteristics. In the low-speed range, the nonlinear characteristics of the contact force are insignificant, and the system vibration is dominated by single-period impact vibration induced by the eccentric force. When the speed increases to a certain level, the contact force dominates the system vibration, and its nonlinearity leads to chaotic system motion. When the speed is sufficiently high, the contact force is much less than the eccentric force, causing the system to finally return to single-period motion.

The Fig. 4 presents the vibration response at a speed of 4000 rpm, corresponding to ball defect sizes of 0.15 mm, 0.3 mm and 0.6 mm respectively. It can be clearly observed from the diagrams that at the same speed, a larger defect size results in more distinct impact waveforms and higher amplitudes. This is because a larger defect size induces stronger TVD excitation, which contributes to more obvious impact waveforms. As indicated in the frequency-domain spectra, besides the rotational frequency f_s, the ball fault frequency f_b and cage fault frequency f_c are also identified. The appearance of the cage fault frequency is ascribed to the impact that the ball-defective area imposes on the cage. This impact forces alterations in the cage's motion trajectory, thus resulting in the emergence of the cage fault frequency. However, considering the influence of eccentricity, the amplitude of f_s still dominates. For the three different ball defect sizes, the theoretically calculated values for f_s, f_c, and f_b are 66.67 Hz, 28.65 Hz and 449.77 Hz respectively. In contrast, when the ball fault size is 0.15mm, the simulation results show that the f_s frequency is 66.67 Hz, the f_c frequency is 29.25 Hz, and the value deviates from the theoretical calculation by 0.6 Hz.

4. Experimental Verification

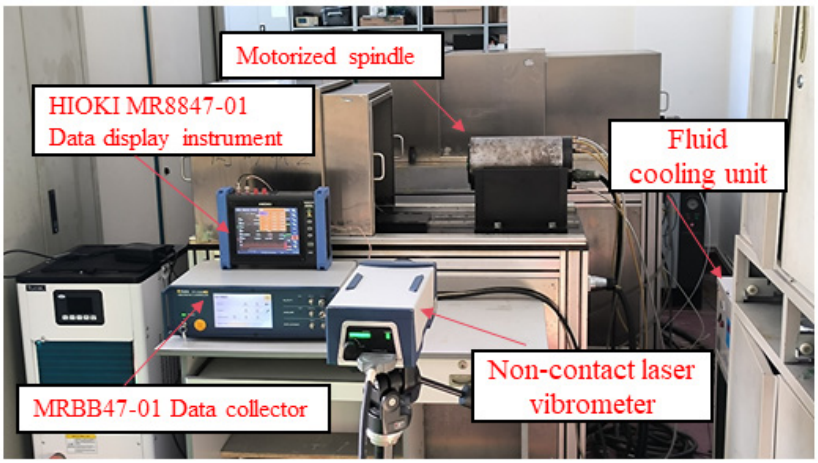

Fig 5. Experimental platform

To verify the reliability of the model, Figure 7 shows the built vibration experimental platform for the motorized spindle. A customized motorized spindle (HT-170-20000-11) was selected as the test object. The front end of the spindle was supported by a healthy 7012CE bearing, while the rear end adopted a 7009CE bearing with a ball defect. A laser vibration measurement system was employed to acquire vibration signals, which mainly comprises a laser vibrometer, a data acquisition instrument, and a data display unit. The laser emitted by the laser vibrometer was directed at the shaft to perform vibration tests. Vibration measurements were conducted

ISSN: 2688-8645

at speed of 6000 rpm, and the measured vibration signals were compared with the corresponding simulation results.

Fig. 6 presents the comparison of vibration signals between experiment and simulation at speed of 6000 rpm. The discrepancy between the experimental and simulated data arises from uncontrollable variables during the experimental process. The frequency spectra mainly exhibit three fundamental frequencies, namely the rotational frequency f_s, ball fault frequency f_b, and cage fault frequency f_c, along with their harmonic components. The calculated values of these three fundamental frequencies are listed in table 2. It is evident that the f_s of the experimental is 100.22 Hz, with a deviation of 0.23 Hz from the simulated value. The f_c in the experiment is 43.15 Hz, showing a deviation of 0.41 Hz from the simulated result. The f_b in the experiment is 674.03 Hz, with a deviation of 2.54 Hz relative to the simulation. The amplitude of f_s in the simulation is 5.11 mm/s, while that in the experiment is 5.36 mm/s, corresponding to a difference of 0.25 mm/s and a relative error of 4.9%. The fundamental frequencies obtained via numerical simulation are in excellent accordance with the experimental findings, thereby confirming the reliability of the theoretical model.

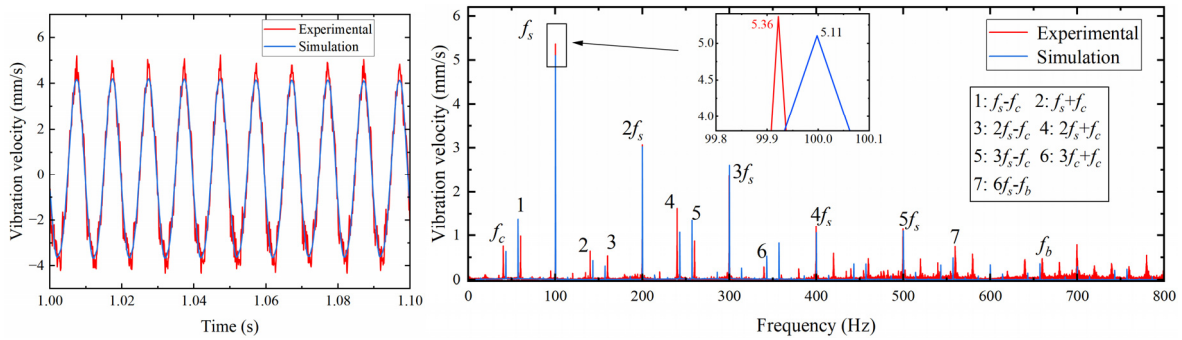

(a) time domain (b) frequency domain

Fig 6. Comparison of experimental and simulation results

Table 2. The characteristic frequencies of the 7009C bearing

Parameters	Theory	Simulation	Experiment
Speed (rpm)	6000	6000	6000
rotational frequency f_s (Hz)	100	99.99	100.22
ball fault frequency f_b (Hz)	673.63	671.49	674.03
cage fault frequency f_c (Hz)	42.36	42.74	43.15

5. CONCLUSION

To investigate the effect of ball defects on the dynamic characteristics of the BRS, a dynamic model of the BRS with ball defects is proposed. The model incorporates the TVD induced by a ball defect, and analyzes the nonlinear vibration responses of the BRS under different speeds and ball defect sizes. The conclusions of this study are summarized as follows:

(1) With the increase in speed, the time-domain waveforms clearly demonstrate a transition trend of the system from single-period motion to multi-period motion. As the speed of the system increases, the system vibration becomes increasingly disordered, and the simultaneous increase in speed and defect size accelerates this transition toward disorder.

(2) At the same speed, a larger defect size results in more distinct impact waveforms and higher amplitudes. As can be seen from the frequency spectra, in addition to the rotational frequency f_s, the cage fault frequency f_c and ball fault frequency f_b are also identified.

Acknowledgments

This work supported by Key Project of the Science and Technology Innovation and Entrepreneurship Fund of China Coal Technology and Engineering Group (2024-ZD003), the Shenyang Young and Middle-aged Science and Technology Innovation Talents Support Program (Grant Nos. RC230970).

References

[1] R Manikandan, Rajasekhara Reddy Mutra. “A comprehensive review on crack detection schemes and modelling techniques in high-speed rotor systems”, Australian Journal of Mechanical Engineering, 2025, Vol. 23 (4), p720-743.

[2] Logamurthi Raja Moorthi, Jawaid Iqbal Inayat-Hussain, Azrul Abidin Zakaria. “Effect of bearing wear on linear and nonlinear responses of a rigid rotor supported by journal bearings”, Journal of Mechanical Science and Technology, 2024, Vol. 38 (6), p2741-2747.

[3] Jing Liu, Linfeng Wang, Zhifeng Shi. “Dynamic modelling of the defect extension and appearance in a cylindrical roller bearing”, Mechanical Systems and Signal Processing, 2022, 173, 109040.

[4] Hongrui Cao, Shuaiming Su, Xin Jing, et al. “Vibration mechanism analysis for cylindrical roller bearings with single/multi defects and compound faults”, Mechanical Systems and Signal Processing, 2020, 144, 106903.

[5] Sachin P Patel, S H Upadhyay. “Influence of roller defect and coupled roller-inner-outer race defects on the performance of cylindrical roller bearing”, Proceedings of the Institution of Mechanical Engineers Part K-Journal of Multi-Body Dynamics, 2019, Vol.233 (3), p731-746.

[6] Yunlong Li, Zhinong Li, Deqiang He, et al. “Effect of clearance on the dynamic characteristics of high-speed rolling bearings with multiple defects”, Mechanical Systems and Signal Processing, 2023, 200,110512.

[7] Mufazzal Sameera, Muzakkir S M, Khanam Sidra. “A dynamic model for simulating vibration response of ball bearings with extended outer race defects for precise spall size estimation”, Journal of Sound and Vibration, 2023, 552, 117606.